Supplementary information

Promoting electrochemical water oxidation kinetics and inhibiting by-product production by employing half metallic material chiral Fe_3O_4

Wenyan Zhang[a,*], *Chaoqun Jiang*[a], *Hangmin Guan*[a], *Yuanyuan Wang*[a], *Yingfei Hu*[a], *Wei Wang*[a], *Wenjie Tian*[a], *Lingyun Hao*[a]

[a] College of Material Engineering, Jinling Institute of technology, Nanjing 211169, China

1. Experiments

1.1 Synthesis of chiral Fe_3O_4

Here, chiral Fe_3O_4 film was coated on FTO through an electrochemical deposition routine with chiral electrolyte that contained L-tartaric acid to direct the chirality. This method was proposed by Switzer et al [S1,S2]. It is a time-effective method with low cost. During the process of electrochemical deposition, chirality was transferred from chiral organic molecules to inorganic solid substance [S1,S2]. The electrolyte employed for the electrochemical deposition of chiral Fe_3O_4 contained 0.1 M Fe (II) ions ($FeSO_4 \cdot 7H_2O$, Sigma Aldrich, purity ≥ 99.0%), 0.1 M L-tartaric acid (Sigma Aldrich, purity ≥ 99.5%), and 0.16 M NaOH (Sigma Aldrich, purity ≥ 98%). In the electrolyte, the Fe^{2+} ions reacted with tartaric acid to form chiral complexes of Fe-tartrate. The Electrodeposition process was conducted at the potential of -1.5 V (vs SCE) for 30s.

1.2 Synthesis of normal Fe_3O_4

The fabrication of normal Fe_3O_4 on FTO was carried out by electrochemical deposition. The aqueous electrolyte for electrochemical deposition involved 0.1 M Fe (II) ions ($FeSO_4 \cdot 7H_2O$, Sigma Aldrich, purity ≥ 99.0%). Typically, electrodeposition process was conducted on FTO substrates at the potential of -1.5 V (vs SCE) for 30s. After electrochemical deposition, the FTO was treated at 600°C for 4h in air atmosphere so that the substance coated on FTO was converted to Fe_2O_3. Fe_2O_3 on FTO was then reduced to Fe_3O_4 by reduction stage at 350 °C in H_2 atmosphere for 2h.

2. Characterization

2.1 Structure and elements analysis

X-ray diffraction (XRD) patterns of the samples were obtained from a Rigaku B/Max-RB diffractometer, recorded with a nickel filtrated Cu Kα radiation operated at 40 kV and 40 mA. X-ray photoelectron spectroscopic measurements of the samples was obtained with a VG Scientific ESCALAB 210-XPS photoelectron spectrometer. During survey scans, the pass energy was 100 eV and the energy step was 1 eV. For high resolution scanning, the pass energy was 30 eV and the energy step was 0.05 eV energy step. In order to remove the moisture and adsorbed impurity on their surface, we evacuated the samples for 24 h before loading them into XPS chamber. UV-Vis Diffraction Reflectance Spectra (DRS) of the samples were recorded by a Shimadzu UV-2600i UV/Visible spectrophotometer. During electrochemical characterization, the electrolyte was 0.1 M KOH solution, with calomel as the reference electrode and Pt foil as counter electrode. Polarized optical microscopic (POM) image of the surface of chiral Fe_3O_4 was conducted in reflection mode, recorded with the polarizers in a parallel orientation or perpendicular arrangement.

2.2 Chirality detection via electrochemical Selectivity

Considering that electrochemical selectivity test represents a sensitive and convenient approach for characterizing the chirality of solid surface materials, we employed electrochemical selectivity experiments to elucidate the surface chirality of Fe_3O_4 film on FTO substrates [S3,S4]. According to these relevant literature, we conducted electrochemical selectivity assessments by performing cyclic voltammetry in aqueous chiral electrolytes. Specifically, we employed a 0.1 M NaOH solutions containing 10 mM L-tartaric acid and 10 mM D-tartaric acid, respectively, as the chiral electrolytes. These experiments were conducted under room temperature conditions with a scanning rate of 50 mV/s.

2.3 H_2O_2 yield measurement

H_2O_2 yield was checked by spectrophotometric titration of the used electrolytes from the reaction system [S5,S6]. O-tolidine served as the redox indicator because H_2O_2 has the

capability to oxidize o-tolidine, resulting in the formation of a two-electron oxidation product with a distinctive yellow color. This product exhibits a characteristic absorption peak at approximately 436 nm. The procedure for measuring H_2O_2 formation involves the following steps, Initially, a constant potential of 1.5 V (vs SCE) was applied to the electrode for 60 minutes in a 0.1 M Na_2SO_4 electrolyte. Subsequently, 1 mL of o-tolidine was mixed with 4 mL of the electrolyte obtained from the reaction system. After 30 minutes, the absorption spectrum of the mixture was recorded using a Shimadzu UV-2600i UV/Visible spectrophotometer.

3. Hydrogen production of water splitting system with chiral Fe_3O_4 film as OER electrocatalyst

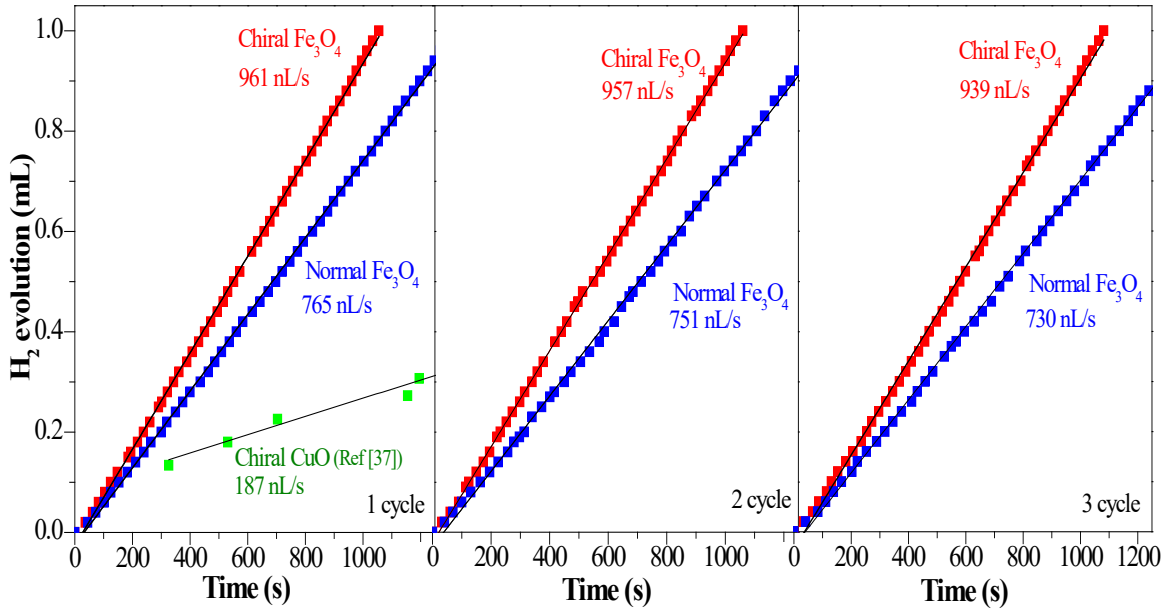

Fig. S1 Three experimental trials of hydrogen production in a water splitting system with the chiral Fe_3O_4 and the normal Fe_3O_4 as OER catalyst at room temperature (conducted at the voltage of 1.5 V (vs SCE), 0.1M KOH as electrolyte, calomel as reference, Pt wire as counter)

Fig. S1 shows the hydrogen production recorded in a water splitting system with chiral Fe_3O_4 film and normal Fe_3O_4 film as OER catalyst. Chiral Fe_3O_4 and normal Fe_3O_4 both exhibited stable performance during the tests of three experimental trials. The hydrogen production rate was calculated. During the three experimental trials, hydrogen production rate with chiral Fe_3O_4 film as OER catalyst was more than 930 nL/s, approximately 20% higher than that with normal Fe_3O_4 film as OER electrocatalyst.

4. Mott–Schottky equation

Mott–Schottky measurement is applied to investigate the charge transport behavior of materials.

The Mott–Schottky relationship is presented in Equation (S1).

$$(C_{sc})^{-2} = 2(E - E_{fb} - kT/e)/(\varepsilon\varepsilon_0 A^2 e N_d) \qquad (S1)$$

Here, N_d represents the free charge carrier densities, ε refers to related to the relative dielectric constant of the anodic film, ε_0 refers to the permittivity of free space, e is the charge of an electron, A means the electrode surface, E_{fb} represents flat band potential, k is the Boltzmann constant, and T is the temperature [S7,S8].

Equation (S1) demonstrates that linear segments slope of Mott–Schottky plots is equal to $2/(\varepsilon\varepsilon_0 A^2 e N_d)$. It can be calculated that the free charge carrier density (N_d) was improved about 10 times in the chiral Fe_3O_4 film as compared with normal Fe_3O_4 film, since the slope of linear segments was 2.03 for normal Fe_3O_4 and decreased to 0.19 for the chiral Fe_3O_4 (as shown in Fig. 7(b) of the main manuscript). This result indicates that chiralization of Fe_3O_4 played an essential role in charge separation and carriers migration around Fe_3O_4.

5. POM

In support of electrochemical selectivity tests, the surface chirality of Fe_3O_4 was clarified by the polarized optical microscopic (POM) measurement conducted under reflection mode. The POM images of FTO surface (Fig. S2(a1,a2)) and bare glass (Fig. S2(b1,b2)) were collected to compare with the POM images of FTO coated with chiral Fe_3O_4 film It can be seen from Fig. S2(a1,a2) and Fig. S2(b1,b2) that in terms of bare FTO and glass, the visual field was bright yet no obvious surface texture could be observed when the polarizers in POM microscope were in a parallel orientation (||), while the visual field became totally dark if the polarizers were perpendicularly arranged (⊥). This result verified that the surface of FTO and bare glass did not have dissymmetric optical activity. In contrast, whether the polarizers in POM were oriented parallelly or perpendicularly, surface texture were obviously shown in the POM images of chiral Fe_3O_4 film (see Fig. S2(c1,c2)). Furthermore, the surface texture images captured from parallelly oriented polarizers and perpendicularly -oriented polarizers was clearly different, when comparing Fig. S2(c1) with Fig. S2(c2). These

evidence suggest highly anisotropic structure with dissymmetric optical activity WAS formed on the surface of chiral Fe_3O_4 film [S9, S10, S11].

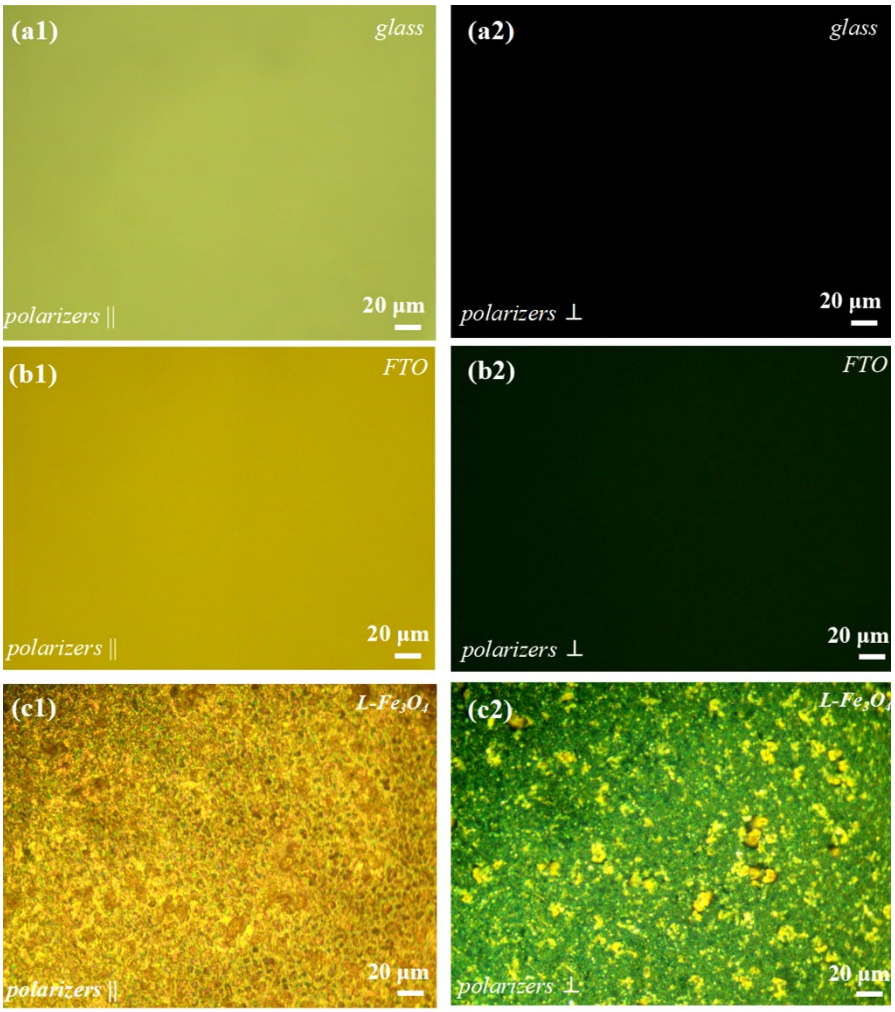

Fig. S2 Polarized optical microscopic (POM) image of the surface of glass, FTO, L-Fe_3O_4 and (b) D-Fe_3O_4 (a1) glass, polarizers in a parallel orientation (||), (a2) glass, polarizers in a perpendicularly orientation (⊥) (b1) FTO, polarizers in a parallel orientation (||), (b2) FTO, polarizers in a perpendicularly orientation (⊥) (c1) L-Fe_3O_4, polarizers in a parallel orientation (||), (c2) L-Fe_3O_4, polarizers in a perpendicularly orientation (⊥)

6. UV-Vis Diffraction Reflectance Spectra (DRS) of the samples

Fig. S3 shows the DRS of the chiral Fe_3O_4 film and the normal Fe_3O_4 film. The chiral Fe_3O_4 exhibited enhanced light absorption at visible-light region as compared with FTO, which suggests the coating of Fe_3O_4 film on the surface of FTO.

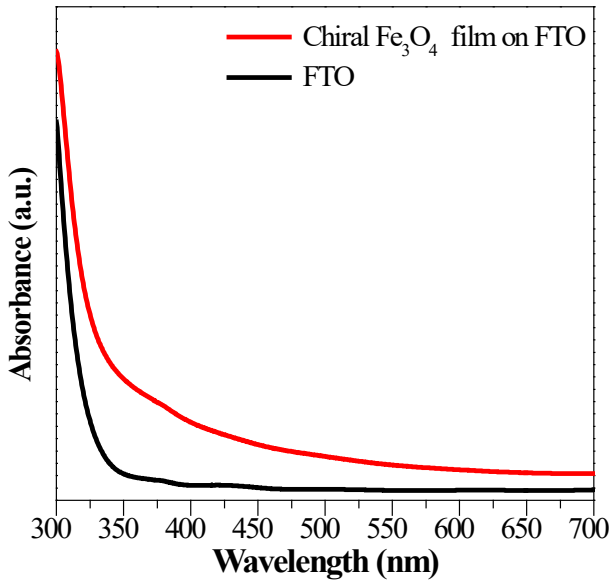

Fig. S3 UV-Vis DRS of chiral Fe_3O_4, and FTO

7. The stability of the chiral Fe_3O_4 film for OER

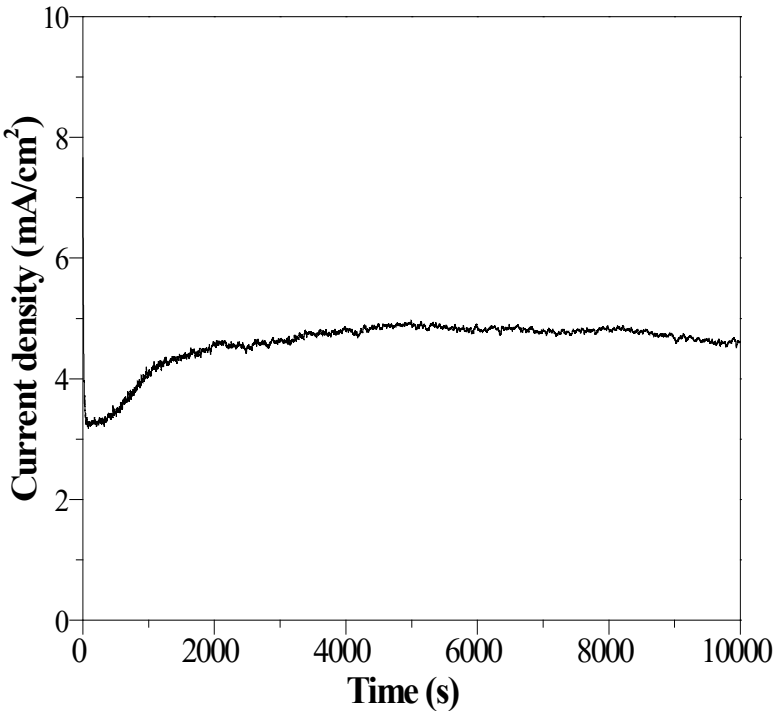

Fig. S4 The stability test of the chiral Fe_3O_4 film for OER at 1.5 V potential (vs SCE)

The stability of the chiral Fe_3O_4 film was checked in aqueous solution of 0.1 M KOH at a potential of 1.5 V. As shown in Fig. S4, the chiral Fe_3O_4 film exhibited relatively stable performance during 10000 s. Besides, the hydrogen production of three experimental trials also indicates the robustness of the chiral Fe_3O_4 film for OER.

8. The morphology of the chiral Fe_3O_4 film after cycling

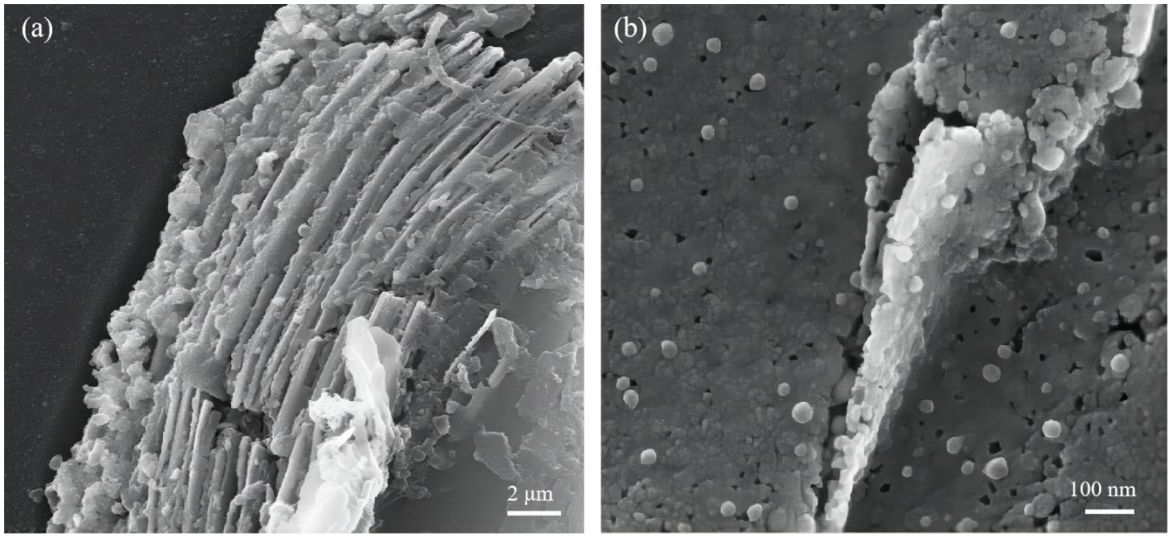

Fig. S5 (a) The SEM image of the chiral Fe_3O_4 film after cycling (b) Magnification image of the SEM image shown in **Fig. S5** (a)

Fig. S5 shows the morphology of the chiral Fe_3O_4 film after cycling. Compared with the its morphology before cycling (as shown in Fig. 3), the surface of the chiral Fe_3O_4 film after cycling became a little rough as some nano particles were released from the film.

9. Comparing the activity of chiral Fe_3O_4 with other metal oxide catalysts

The influence on current density in oxygen evolution reaction (OER) is not solely attributed to the intrinsic activity of the catalyst but is significantly affected by other factors such as the substrate supporting the catalyst and the electrolyte utilized. For example, the catalyst demonstrates notably higher current density supported by Ni foam instead of the FTO glass substrates. This disparity arises from the 3D porous structure of Ni foam, which offers a larger surface area for OER compared to the FTO surface. Furthermore, owing to its metallic nature, Ni foam exhibits superior conductivity to FTO. Furthermore, the selection of electrolyte significantly impacts the current density of a catalyst. For instance, a catalyst typically demonstrates an increased current density in a 1 M KOH solution compared to a 0.1 M KOH electrolyte.

As a result, to thoroughly evaluate the oxygen evolution reaction (OER) activity of diverse catalysts, this study incorporates information about their substrates and the

electrolytes utilized for OER, along with their corresponding overpotential at 10 mA/cm^2 (η_{10}) and Tafel slope, as presented in Tab. S1.

Moreover,

It is worth noting that this research primarily concentrates on elucidating the impact of spin alignment on facilitating the OER process for the catalyst by introducing structural chirality to induce the ***CISS*** effect to make the spin aligning available. Thereby, though there are so much metal oxide catalysts with outstanding performance, Tab. S1 just provides a concise summary of spin-related metal oxide catalysts and chiral catalysts designed to enhance the OER. As shown in Tab. S1, the overpotential of chiral Fe_3O_4 is higher than that of some spin-related metal oxides and chiral catalysts. Nevertheless, the activity of chiral Fe_3O_4 film surpasses that of its counterparts, such as the ferromagnetic $ZnFe_2O_4$ and normal Fe_3O_4 (see Tab. S1). This observation underscores that the ***CISS*** effect and the half-metallic nature of the chiral Fe_3O_4 film coordinated to boost its activity for OER.

Tab. S1 The catalytic performance of chiral Fe_3O_4 and typical spin related metal oxide catalysts or chiral catalysts for facilitating the oxygen evolution reaction (OER)

Catalyst	**Overpotential (≥10 mA/cm^2)**	**Tafel slope**	**Substrate**	**Electrolyte**	**Ref**
Chiral Fe_3O_4	η_{10} = 780 mV	120 mV/dec	FTO	0.1 M KOH	This work
Chiral CuO	Did not reach 10 mA/cm^2	—	FTO	0.1 M KOH	[37]
Normal Fe_3O_4	η_{10} = 930 mV	224 mV/dec	FTO	0.1 M KOH	This work
Chiral Fe_3O_4 nanoparticles	Did not reach 10 mA/cm^2	92.3 mV/dec	Glassy carbon electrode	1 M KOH	[S12]
Ferromagnetic $ZnFe_2O_4$	Did not reach 10 mA/cm^2	—	Ti foil	0.1 M KOH	[S13]
Chiral CoO_x Thin Film	η_{10} = 500 mV	—	FTO	0.1 M KOH	[S14]
Chiral CoO_x Thin Film	Did not reach 10 mA/cm^2	—	FTO	Na_2CO_3/$NaHCO_3$ aqueous solution (pH 10)	[S14]
CdSe coupled with chiral monolayer	Did not reach 10 mA/cm^2	—	FTO	Na_2SO_3/Na_2S aqueous solution (pH 9.5)	[29]
TiO_2 coated with chiral monolayer	Did not reach 10 mA/cm^2	—	FTO	0.1 M Na_2SO_4	[32]
$Co_{3-x}Fe_xO_4$ spinel oxides	Did not reach 10 mA/cm^2	—	Glassy carbon electrodes	1 M KOH	[S15]

Ferromagnetic – antiferromagnetic Fe_3O_4@$Ni(OH)_2$ core–shell catalysts	η_{10} = 325 mV	64.3 mV/dec	Carbon paper electrode	1 M KOH	[S16]
$ZnCo_xMn_{2-x}O_4$	η_{10} = 570 mV	51 mV/dec	Rotating disk electrode	0.1 M KOH	[S17]
Chiral $Co_{3-x}Fe_xO_4$	η_{10} = 320 mV	34 mV/dec	Glassy carbon electrodes	1 M NaOH	[S18]
Double perovskite $PrBaCo_2O_6$ (PBCO)	Did not reach 10 mA/cm^2	92 mV/dec	$SrTiO_3$	0.1 M KOH	[S19]
$ZnCo_2O_4$	Did not reach 10 mA/cm^2	—	Glassy carbon electrodes	1 M NaOH	[S20]
Magnetic $Co_2Mo_3O_8$@NC (single-crystal $Co_2Mo_3O_8$/ultrathin nitrogen-rich carbon)	η_{10} = 320 mV	87.5 mV/dec	Glassy carbon electrodes	1 M NaOH	[S21]
Chiral molecules functionalized 2D Ni (NiO_x) and NiFe ($NiFeO_x$) oxo-hydroxides	Did not reach 10 mA/cm^2	—	Au film	0.1 M KOH	[S22]

Reference

[S1] H.M. Kothari, E.A. Kulp, S. Boonsalee, M.P. Nikiforov, E.W. Bohannan, P. Poizot, S. Nakanishi, J.A. Switzer, Chem. Mater., 2004, 16, 4232–4244.

[S2] R. Widmer, F.J. Haug, P. Ruffieux, O. Gröning, M. Bielmann, P. Gröning, R. Fasel, J. Am. Chem. Soc., 2006, 128, 14103–14108.

[S3] E.W. Bohannan, H.M. Kothari, I.M. Nicic, J.A. Switzer, J. Am. Chem. Soc., 2004, 126, 488–489.

[S4] W.Y. Zhang, J. Li, G.X. Lu, H.M. Guan, L.Y. Hao, Chem. Commun., 2019, 55, 13390–13393.

[S5] K.B. Ghosh, W.Y. Zhang, F. Tassinari, Y. Mastai, O. Lidor-Shalev, R. Naaman, P. Möllers, D. Nürenberg, H. Zacharias, J. Wei, E. Wierzbinski, D.H. Waldeck, J. Phys. Chem. C, 2019, 123, 3024–3031.

[S6] W. Mtangi, F. Tassinari, K. Vankayala, A.V. Jentzsch, B. Adelizzi, A.R.A. Palmans, C. Fontanesi, E.W. Meijer, R. Naaman, J. Am. Chem. Soc., 2017, 139, 2794–2798.

[S7] B.A. Koiki, B.O. Orimolade, B.N. Zwane, D. Nkosi, N. Mabuba, O.A. Arotiba, Electrochim. Acta, 2020, 340, 135944.

[S8] A.S. Bondarenko, G.A. Ragoisha, J. Solid State Electrochem., 2005, 9, 845–849.

[S9] C. Wang , J. Li, E. Paineau, A. Laachachi, C. Colbeau-Justin, H. Remita, M.N. Ghazzal, J. Mater. Chem. A, 2020, 8, 10779–10786.

[S10] A. Tran, C.E. Boott, M.J. MacLachlan, Adv. Mater., 2020, 32, 1905876.

[S11] I. Song, J. Ahn, H. Ahn, S.H. Lee, J.G. Mei, N.A. Kotov, J.H. Oh, Nature, 2023, 617, 92–99.

[S12] A.N. Nair, S. Fernandez, M. Marcos-Hernández, D.R. Romo, S.R. Singamaneni, D.Villagran, and S.T. Sreenivasan, Nano Lett., 2023, 23, 9042–9049.

[S13] W.Q. Gao, R. Peng, Y.Y. Yang, X.L. Zhao, C. Cui, X.W. Su, W. Qin, Y. Dai, Y.D. Ma, H. Liu, and Y.H. Sang, ACS Energy Lett., 2021, 6, 2129–2137

[S14] S. Ghosh, B.P. Bloom, Y.Y. Lu, D. Lamont, and D.H. Waldeck, J. Phys. Chem. C, 2020, 124, 22610–22618.

[S15] T.Z. Wu, X. Ren, Y.M. Sun, S.N. Sun, G.Y. Xian, G.G. Scherer, A.C. Fisher, D. Mandler, J.W. Ager, A. Grimaud, J.L. Wang, CM. Shen, H.T Yang, J. Gracia, H.J. Gao, Z.C.J. Xu, Nat. Commun., 2021, 12, 3634.

[S16] J.J. Ge, R.R.X. Chen, X. Ren, J.W. Liu, S.J.H. Ong, Z.C.J. Xu, Adv. Mater., 2021, 2101091.

[S17] SN. Sun, Y.M. Sun, Y. Zhou, J.J. Shen, D. Mandler, R. Neumann, and Z.C.J. Xu, Chem. Mater., 2019, 31, 19, 8106–8111.

[S18] A. Vadakkayil, C. Clever, K.N. Kunzler, S.S. Tan, B.P. Bloom, and D.H. Waldeck, Nature Commu. 2023, 14, 1067.

[S19] C.R. Wu, Y. Sun, Z.N. Yang, J.Y. Hu, T.Y. Ding, J. Cheng, and K.H. L. Zhang, Chem. Mater. 2022, 34, 23, 10509–10516.

[S20] Y.M. Sun, X. Ren, S.N. Sun, Z. Liu, S.B. Xi, and Z.C.J. Xu, Angew. Chem. Int. Ed., 2021, 60, 14536-14544.

[S21] Z.Q. Liu, T. Ouyang, X.T. Wang, X.Q. Mai, A.N. Chen, and Z.Y. Tang, Angew. Chem. Int. Ed., 2020, 59, 11948-11957.

[S22] Y.C. Liang, K. Banjac, K. Martin, N. Zigon, S. Lee, N. Vanthuyne, F.A.Garcés-Pineda, J.R. Galán-Mascarós, X.L. Hu, N. Avarvari, and M. Lingenfelder, Nat. Commun., 2022, 13, 3356.